Deformations and Stability of an Elastica Subjected to an Off-Axis Point Constraint

Jen-San Chen[1]
Professor
e-mail: jschen@ntu.edu.tw

Wei-Chia Ro

Department of Mechanical Engineering,
National Taiwan University,
Taipei 10617, Taiwan

This paper studies, both theoretically and experimentally, the deformation, the vibration, and the stability of a buckled elastic strip (also known as an elastica) constrained by a space-fixed point in the middle. One end of the elastica is fully clamped while the other end is allowed to slide without friction and clearance inside a rigid channel. The point constraint is located at a specified height above the clamping plane. The elastic strip buckles when the pushing force reaches the conventional buckling load. At this buckling load, the elastica jumps to a symmetric configuration in contact with the point constraint. As the pushing force increases, a symmetry-breaking bifurcation occurs and the elastica evolves to one of a pair of asymmetric deformations. As the pushing force continues to increase, the asymmetric deformation experiences a second jump to a self-contact configuration. A vibration analysis based on an Eulerian description taking into account the sliding between the elastica and the point constraint is described. The natural frequencies and the stability of the calculated equilibrium configurations can then be determined. The experiment confirms the two jumps and the symmetry-breaking bifurcation predicted theoretically. [DOI: 10.1115/1.4000426]

1 Introduction

The primary goal of this study on a constrained elastica is to understand the behavior of a thin elastic strip under external compression when it is subjected to lateral constraints. This type of analysis can be considered as an extension of the classical elastica theory initiated by Euler and Lagrange over two centuries ago [1]. For instance, Domokos and co-workers [2,3] investigated the planar buckling patterns of an elastic hinged-hinged bar constrained inside a straight channel with clearance. Plaut et al. [4] studied the deflection and buckling of a bent elastica in contact with a flat surface. Chai [5,6] studied the energy absorption potential of laterally confined bars under monotonically increasing edge displacement. Roman and Pocheau [7] used an elastica model to investigate the post-buckling response of bilaterally constrained thin plates subjected to a height reduction. Chen and co-workers [8,9] studied the deformation of a planar elastica inside a circular channel with clearance. These analyses find applications in a variety of practical problems, such as in nonwoven fabrics manufacturing, electronic circuit strip wiring, and stent deployment procedures.

A constrained elastica is a highly nonlinear problem and most of the abovementioned works focused on finding the deformation patterns when the loading mechanism at the end is prescribed. It is not surprising that for a specific end loading, more than one deformation pattern may exist [9]. In order to be sure that the calculated deformation can be realized and observed in reality, a stability analysis is needed. As far as we know, however, stability analysis on constrained elastica is relatively rare in literature [2].

In this paper we study the deformation pattern and the stability of an elastica constrained by a space-fixed point in the middle with clearance. The point constraint is at a specified distance above the base plane. The elastica is fully clamped on one end and "partially" clamped on the other. The partial clamp is a straight channel with part of the elastica being allowed to slide in it without friction and clearance. This mechanics problem may be encountered when a paper jam occurs in a printer or a photocopy machine. We first study theoretically the deformation patterns and their stabilities of the constrained elastica when the longitudinal pushing force increases. After the buckled elastic strip contacts the point constraint, our theory predicts that a symmetry-breaking bifurcation followed by a jump action will occur. These predictions are then confirmed by experimental observations. The method presented in this paper can be extended to other kinds of lateral constraints, such as straight or curved walls.

2 Problem Description

Figure 1 shows an inextensible elastic strip with the right end fully clamped in point B. On the left hand side there is a straight channel with an opening in point A. The distance between points A and B is L. Part of the strip is allowed to slide without friction and clearance inside the channel. A longitudinal pushing force F_A is applied on the left end of the strip inside the channel causing it to buckle in the domain of interest between points A and B. An xy-coordinate system is fixed at point A. Point H, fixed at positions $x=L/2$ and $y=h$, prevents the elastica from deforming freely after the elastica contacts point H. If the elastic strip buckles downward to the other side of the clamp plane, we assume that there is a similar point constraint on the other side with $y=-h$ (not shown in Fig. 1) and the resulting behavior will be equivalent.

The elastic strip is assumed to be straight and stress-free when $F_A=0$. The effect of gravity is ignored. The strip is uniform in all mechanical properties along its length. The length and the shape of the elastica in the domain of interest vary as the pushing force F_A increases. The boundary condition in point A may be called "partially clamped" by which we mean that the strip is allowed to slide freely through opening A while the lateral displacement and slope in A are fixed. The dashed and solid curves in Fig. 1 represent two typical stages of the elastica deformation when F_A increases beyond the buckling load. The dashed curve is a symmetric deformation pattern before the elastica contacts the point constraint. The solid curve represents an asymmetric deformation after the elastica contacts point H. Other deformation patterns may also exist, which will be discussed later. The purpose of this paper is to study the interaction of the elastica and the point constraint.

[1]Corresponding author.

Contributed by the Applied Mechanics Division of ASME for publication in the JOURNAL OF APPLIED MECHANICS. Manuscript received January 9, 2009; final manuscript received July 30, 2009; published online February 4, 2010. Assoc. Editor: William Screrzinger.

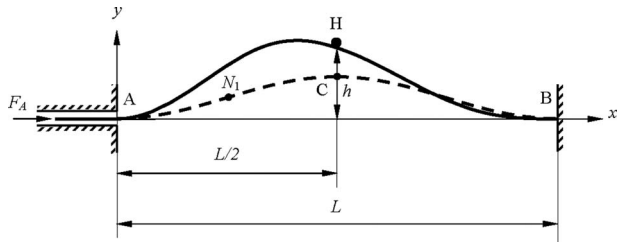

Fig. 1 An elastica constrained by a point at H. The dashed and solid curves represent typical symmetric and asymmetric deformations, respectively.

This study differs from most of the previous works on constrained elastica in two aspects. First of all, in most of the previous works, the elastica is of a fixed length. In this paper the length of the elastica within the domain of interest changes as the external load varies. Other variable-length elastica problems without lateral constraint can be found in Refs. [10–13]. Second, the lateral constraint in this paper is a single point while in previous works the constraint is a wall. A discrete system constrained by off-axis point constraints can be found in Refs. [14,15].

3 Equilibrium Equations and Deformation Patterns

The equilibrium equation at any point (x,y) of the buckled strip between points A and B, as shown in Fig. 1, can be written as

$$EI\frac{d\theta}{ds} = -Q_A x - F_A y + M_A \tag{1}$$

Q_A (positive when pointing downward) and M_A (positive when clockwise) are the internal shear force and bending moment, respectively, provided by the partial clamp in A. θ (positive when counterclockwise) is the rotation angle of the strip in point (x,y). EI is the flexural rigidity of the elastic strip. s is the length of the strip measured from point A. For convenience, we introduce the following dimensionless parameters (with asterisks):

$$(s^*,x^*,y^*) = \frac{(s,x,y)}{L}, \quad (Q_A^*,F_A^*) = \frac{L^2}{4\pi^2 EI}(Q_A,F_A),$$

$$M_A^* = \frac{L}{4\pi^2 EI}M_A$$

$$t^* = \frac{1}{L^2}\sqrt{\frac{EI}{\mu}}t, \quad \omega^* = L^2\sqrt{\frac{\mu}{EI}}\omega \tag{2}$$

where μ is the mass per unit length of the elastica, t is time, and ω is the circular natural frequency, which will be discussed in the dynamic analysis later. After substituting relations (2) into Eq. (1) and dropping all the superposed asterisks thereafter for simplicity, we obtain the dimensionless equilibrium equation

$$\frac{d\theta}{ds} = 4\pi^2(M_A - Q_A x - F_A y) \tag{3}$$

After differentiating Eq. (3) with respect to s and noting the relations $dy/ds = \sin\theta$ and $dx/ds = \cos\theta$, we obtain

$$\frac{d^2\theta}{ds^2} = -4\pi^2(Q_A\cos\theta + F_A\sin\theta) \tag{4}$$

We multiply Eq. (4) by $d\theta$ and integrate to obtain

$$\frac{1}{2}\left(\frac{d\theta}{ds}\right)^2 = 4\pi^2(-Q_A\sin\theta + F_A\cos\theta) + D_A \tag{5}$$

where D_A is an integration constant. From Eq. (5) we can write

$$ds = \frac{\pm d\theta}{U_A} \tag{6}$$

where U_A is defined as

$$U_A = \sqrt{8\pi^2(F_A\cos\theta - Q_A\sin\theta) + 2D_A} \tag{7}$$

From Eq. (6) we obtain

$$dx = \frac{\pm\cos\theta d\theta}{U_A} \tag{8}$$

$$dy = \frac{\pm\sin\theta d\theta}{U_A} \tag{9}$$

The choice of "$\pm$" sign in Eqs. (6), (8), and (9) depends on the curvature of the deflection curve. The "+" sign should be chosen if the curvature is positive and vice versa. In the following sections, we will investigate five specifically assumed deformations.

3.1 Deformation (1): Before Contact. The first deformation pattern after buckling is the symmetric shape before contact, as shown by the dashed curve in Fig. 1. Since the curvatures in point A and the one in midpoint C are of opposite signs, there exists an inflection point N_1 in between. The rotation angle of the elastica in N_1 is denoted by θ_1. Since the shear force $Q_A=0$ in this case, the constant D_A in Eq. (5) can be written as

$$D_A = -4\pi^2 F_A\cos\theta_1 \tag{10}$$

By using Eq. (10), Eqs. (5) and (7) can be rewritten as

$$\frac{1}{2}\left(\frac{d\theta}{ds}\right)^2 = 4\pi^2 F_A(\cos\theta - \cos\theta_1) \tag{11}$$

$$U_A = \sqrt{8\pi^2 F_A(\cos\theta - \cos\theta_1)} \tag{12}$$

After integrating Eq. (8) from point A to midpoint C of the elastica, we obtain the x-coordinate of point C as

$$x_C = \frac{1}{2} = \int_{\theta_A(=0)}^{\theta_1} - \int_{\theta_1}^{\theta_C(=0)} \frac{\cos\theta d\theta}{U_A} \tag{13}$$

The integral notation in Eq. (13) is a simplified expression, meaning that both integrals share the same integrand. Similar notations will be adopted throughout this paper. When the longitudinal force F_A is specified, Eq. (13) can be used to solve for the unknown θ_1.

Once θ_1 is found, the shape of the elastica can be obtained by calculating the (x,y) coordinates of the deformed strip as follows: First of all the rotation angle ϕ of the deflection curve in point A is zero. Before the rotation angle reaches θ_1 we use the formulas

$$x(\phi) = \int_0^{\phi} \frac{\cos\theta d\theta}{U_A}, \quad y(\phi) = \int_0^{\phi} \frac{\sin\theta d\theta}{U_A} \tag{14}$$

After the rotation angle of the deflection curve passes θ_1, the formulas in Eq. (14) must be replaced by

$$x(\phi) = \int_0^{\theta_1} - \int_{\theta_1}^{\phi} \frac{\cos\theta d\theta}{U_A}, \quad y(\phi) = \int_0^{\theta_1} - \int_{\theta_1}^{\phi} \frac{\sin\theta d\theta}{U_A} \tag{15}$$

Equations (14) and (15) give the shape of the left half of the elastica, whose mirror image across point C becomes the shape of the other half. This symmetric deformation is called deformation (1) in this paper.

After determining the shape, the dimensionless length l of the elastica between point A and point B can be calculated as

$$l = \int ds = \left[2\int_{\theta_A(=0)}^{\theta_1} - \int_{\theta_1}^{\theta_C(=0)} \frac{d\theta}{U_A}\right] \tag{16}$$

The length Δl of the elastica being pushed in through the opening

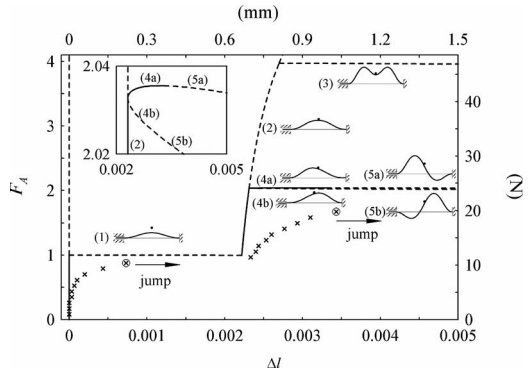

Fig. 2 Load-deflection curve for $h=0.03$. The solid and dashed curves represent stable and unstable deformations, respectively. The cross marks × represent the experimental measurements. The last points before the jumps occur are circled.

is $\Delta l = l - 1$.

In Fig. 2 we show the load-deflection relation between force F_A and length increment Δl for the case when the height of the point constraint $h=0.03$. The deformation (1) is shown on the top of the dashed line, which starts at $(F_A, \Delta l) = (1, 0)$ and ends at (0.99668,0.0022188). The slope of this load-deflection curve is slightly negative. The dashed and solid curves on this load-deflection plane represent unstable and stable configurations, respectively. The procedure to determine the stability of the elastica will be discussed in latter sections.

3.2 Deformation (2): 1-1 Symmetric. After the middle point C of the elastica touches the point constraint H, the deformation pattern initially remains symmetric, called deformation (2). The notation "1-1 symmetric" indicates that there is one inflection point in each half span of the elastica. In this case the shear force Q_A is no longer zero. Therefore, Eqs. (10)–(12) are replaced by

$$D_A = -4\pi^2(F_A \cos\theta_1 - Q_A \sin\theta_1) \tag{17}$$

$$\frac{1}{2}\left(\frac{d\theta}{ds}\right)^2 = 4\pi^2[F_A(\cos\theta - \cos\theta_1) - Q_A(\sin\theta - \sin\theta_1)] \tag{18}$$

$$U_A = \sqrt{8\pi^2[F_A(\cos\theta - \cos\theta_1) - Q_A(\sin\theta - \sin\theta_1)]} \tag{19}$$

The point constraint restricts the elevation of midpoint C at

$$y_C = h = \int_{\theta_A(=0)}^{\theta_1} - \int_{\theta_1}^{\theta_C(=0)} \frac{\sin\theta d\theta}{U_A} \tag{20}$$

After solving Eqs. (13) and (20) simultaneously for the two unknowns Q_A and θ_1, the shape of the elastica can be obtained for a given F_A as in the last subsection. The load-deflection curve of deformation (2) starts at $(F_A, \Delta l) = (0.99668, 0.0022188)$ and ends at (3.97314,0.0026985). It is noted that the lower part of this load-deflection curve up to (2.03268,0.0023129) is solid and the upper part is dashed. At the point separating the solid and dashed parts, a symmetry-breaking bifurcation occurs and the elastica evolves to a pair of asymmetric deformations as will be discussed later.

3.3 Deformation (3): 2-2 Symmetric. As the pushing force continues to increase, it is natural to envision that the elastica may evolve to an "M" shape, i.e., there exist two inflection points in each half of the span, as shown by deformation (3) in Fig. 2. The rotation angles at the two inflection points in the left half span are denoted by θ_1 and θ_2. For this deformation, Eqs. (13) and (20) are rewritten as

$$x_C = \frac{1}{2} = \int_{\theta_A(=0)}^{\theta_1} - \int_{\theta_1}^{\theta_2} + \int_{\theta_2}^{\theta_C(=0)} \frac{\cos\theta d\theta}{U_A} \tag{21}$$

$$y_C = h = \int_{\theta_A(=0)}^{\theta_1} - \int_{\theta_1}^{\theta_2} + \int_{\theta_2}^{\theta_C(=0)} \frac{\sin\theta d\theta}{U_A} \tag{22}$$

where U_A is defined in Eq. (19). From the condition $d\theta/ds|_{\theta=\theta_2} = 0$ and Eq. (18), we obtain

$$Q_A = \frac{F_A(\cos\theta_2 - \cos\theta_1)}{(\sin\theta_2 - \sin\theta_1)} \tag{23}$$

After substituting Eq. (23) into Eqs. (21) and (22), we can solve Eqs. (21) and (22) simultaneously for the two unknowns θ_1 and θ_2 for a given F_A. The shape of the elastica can then be determined similarly as in previous subsections. The load-deflection curve corresponding to deformation (3) starts at $(F_A, \Delta l) = (3.97314, 0.0026985)$ and continues beyond the range of Fig. 2. The slope of this curve is slightly negative. It will be shown that this symmetric deformation is also unstable. It is noted that at the bifurcation point $(F_A, \Delta l) = (3.97314, 0.0026985)$ there is another branch, which continues almost vertically beyond the range of Fig. 2. The deformation corresponding to this branch is 3-3 symmetric and unstable. We will not follow this branch further in this paper.

3.4 Deformation (4): 1-1 Asymmetric. At point $(F_A, \Delta l) = (2.03268, 0.0023129)$, the symmetric deformation (2) described previously may bifurcate to a pair of asymmetric deformations, which involve one inflection point in each of the two subdomains AH and HB; see the solid curve in Fig. 1 and the curves (4a) and (4b) in Fig. 2. The rotation angles on these two inflection points are denoted by θ_1 (in AH) and θ_2 (in HB), respectively. Similar to the procedure in Sec. 3.2, two geometric conditions are obtained for the elastica in the subdomain AH

$$x_H = \frac{1}{2} = \int_{\theta_A(=0)}^{\theta_1} - \int_{\theta_1}^{\theta_H} \frac{\cos\theta d\theta}{U_A} \tag{24}$$

$$y_H = h = \int_{\theta_A(=0)}^{\theta_1} - \int_{\theta_1}^{\theta_H} \frac{\sin\theta d\theta}{U_A} \tag{25}$$

where θ_H is the rotation angle of the elastica at the contact point H. U_A is defined in Eq. (19). In subdomain HB the geometric conditions can be written as

$$x_B = 1 = \frac{1}{2} - \int_{\theta_H}^{\theta_2} + \int_{\theta_2}^{\theta_B(=0)} \frac{\cos\theta d\theta}{U_B} \tag{26}$$

$$y_B = 0 = h - \int_{\theta_H}^{\theta_2} + \int_{\theta_2}^{\theta_B(=0)} \frac{\sin\theta d\theta}{U_B} \tag{27}$$

where

$$U_B = \sqrt{8\pi^2[F_B(\cos\theta - \cos\theta_2) - Q_B(\sin\theta - \sin\theta_2)]} \tag{28}$$

F_B and Q_B are the longitudinal pushing force and the shear force at fixed end B, respectively.

We assume that there is no friction between the point constraint and the elastica. As a consequence, the point constraint exerts a force normal to the elastica in point H. This constraint equation can be written as

$$F_B - F_A = (Q_B - Q_A)\tan\theta_H \tag{29}$$

Furthermore, the continuity in curvature at point H can be stated mathematically as

$$F_A(\cos\theta_H - \cos\theta_1) - Q_A(\sin\theta_H - \sin\theta_1) = F_B(\cos\theta_H - \cos\theta_2) - Q_B(\sin\theta_H - \sin\theta_2) \tag{30}$$

The six equations, Eqs. (24)–(27), (29), and (30), can be used to solve for the six unknowns θ_1, θ_2, θ_H, Q_A, F_B, and Q_B simultaneously for a given F_A.

It is noted that for the set of six equations there exist two different solutions. Unlike the symmetric deformations, the end compressive forces F_A and F_B can be different for asymmetric deformations. If (F_A, Q_A, θ_1) exchanges with, $(F_B, Q_B, -\theta_2)$, the same set of equations can be satisfied. Therefore, there exist a pair of deformations (4a) and (4b) as shown in Fig. 2; one is the mirror image of the other across the point constraint. The load-deflection curves of these two solutions are different and slightly separated in Fig. 2. If the vertical axis were F_A for one of the curves and F_B for the other one, the curves would be identical. Both curves of (4a) and (4b) start at $(F_A, \Delta l) = (2.03268, 0.0023129)$ while (4a) ends at (2.03545, 0.0028996) and (4b) ends at (2.02600 0.0028996). The slopes of curves (4a) and (4b) are positive and negative throughout, respectively. Stability analysis later indicates that deformation (4b) is unstable while (4a) is stable.

3.5 Deformation (5): 2-1 and 1-2 Asymmetric. As Δl increases further, the pair of deformations (4a) and (4b) evolve to a pair of asymmetric deformations (5a) and (5b), as shown in Fig. 2. For (5a), which is also known as 2-1 asymmetric, the rotation angles of the two inflection points in AH are θ_1 and θ_3 and the rotation angle of the inflection point in HB is θ_2. The two geometric conditions obtained for the elastica in the subdomain AH can be updated to

$$x_H = \frac{1}{2} = -\int_{\theta_A(=0)}^{\theta_1} + \int_{\theta_1}^{\theta_3} - \int_{\theta_3}^{\theta_H} \frac{\cos\theta d\theta}{U_A} \tag{31}$$

$$y_H = h = -\int_{\theta_A(=0)}^{\theta_1} + \int_{\theta_1}^{\theta_3} - \int_{\theta_3}^{\theta_H} \frac{\sin\theta d\theta}{U_A} \tag{32}$$

where U_A is defined in Eq. (19). We can now use the seven equations, Eqs. (26), (27), (29)–(32), and (23) (with θ_2 in Eq. (23) being replaced by θ_3) to solve for the seven unknowns θ_1, θ_2, θ_3, θ_H, Q_A, F_B, and Q_B simultaneously for a given F_A. For deformation (5a), the top is in the subdomain AH while the trough is in the subdomain HB. If the deformation is reflected with respect to the point constraint, the other pattern (5b) is obtained. The slope of load-deflection curve of (5b) is negative throughout. On the other hand, the curve of (5a) is of convex shape with the top being at point $(F_A, \Delta l) = (2.03554, 0.0031711)$, which is very close to the end of curve of deformation (4a). Deformation (5a) is stable first until the curve reaches the top at $(F_A, \Delta l) = (2.03554, 0.0031711)$. At this critical point, the elastica will jump to another configuration. The load-deflection curves near the symmetry-breaking point are magnified and shown in the inset of Fig. 2. It is noted that the prediction of the symmetry-breaking bifurcation, the asymmetric deformations, and the second jump can only be predicted with the nonlinear elastica model even if the off-axis distance h is merely 0.03 as in Fig. 2. The linear analysis, however, can predict the first jump and the symmetric deformation when h is small.

The theoretical load-deflection curves shown in Fig. 2 give us a mental picture how the elastica evolves as the pushing force F_A increases. First of all, the elastica remains still when F_A is smaller than 1, the Euler buckling load. As soon as F_A reaches 1, the elastica jumps to symmetric deformation (2) in contact with the point constraint. As F_A increases, a symmetry-breaking bifurcation occurs and the elastica evolves to asymmetric deformation (4a) first and smoothly to (5a). As F_A continues to increase up to a certain value, a second jump occurs. Following this jump the elastica will eventually settle to a self-contact configuration. This self-contact configuration requires a length increment Δl over 8, which is well beyond the range of Fig. 2 and will be neglected in this paper.

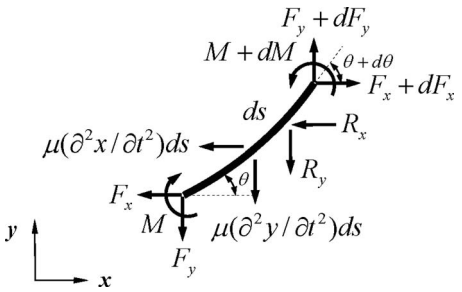

Fig. 3 The free body diagram of a small element *ds* constrained by the space-fixed point

4 Vibration and Stability Analyses

4.1 Lagrangian and Eulerian Descriptions. As mentioned above, the deformation patterns discussed in Sec. 3 may not necessarily be stable. If the deformation is unstable, then it cannot be realized in reality. In order to study the vibration and stability properties of the elastica, we first derive the equations of motion of a small element ds supported by the point constraint, as shown in Fig. 3. $F_x(s,t)$ and $F_y(s,t)$ are the internal forces in the x- and y-directions. The inextensibility of the elastica can be stated mathematically as

$$\frac{\partial x(s,t)}{\partial s} = \cos\theta(s,t) \tag{33}$$

$$\frac{\partial y(s,t)}{\partial s} = \sin\theta(s,t) \tag{34}$$

The balance of moment and forces in the x- and y-directions results in

$$\frac{\partial M(s,t)}{\partial s} = F_x(s,t)\sin\theta(s,t) - F_y(s,t)\cos\theta(s,t) \tag{35}$$

$$\frac{\partial F_x(s,t)}{\partial s} - R_x(t)\,\delta(s - l_1 - \eta_1(t)) = \frac{1}{4\pi^2}\frac{\partial^2 x(s,t)}{\partial t^2} \tag{36}$$

$$\frac{\partial F_y(s,t)}{\partial s} - R_y(t)\,\delta(s - l_1 - \eta_1(t)) = \frac{1}{4\pi^2}\frac{\partial^2 y(s,t)}{\partial t^2} \tag{37}$$

The moment-curvature relation from the Euler–Bernoulli beam model is

$$\frac{\partial\theta(s,t)}{\partial s} = 4\pi^2 M(s,t) \tag{38}$$

The readers are reminded that the functions x, y, θ, M, F_x, and F_y in Eqs. (33)–(38) are dimensionless and are all written explicitly in terms of s and t for clarity. These six equations can be called the Lagrangian version of the governing equations because a material element ds at location s is isolated as the free body. s may be called the Lagrangian coordinate of a point on the elastica.

It is noted that $s=0$, l_1, and l represent the material points on the left end, the contact point, and the right end, respectively, when the elastica is in equilibrium. During vibration, the elastica may "slide" on the point constraint. As a consequence, the contact point on the elastica may change from $s=l_1$ to $s=l_1+\eta_1$, where $\eta_1(t)$ is a small number. This change in contact point is reflected in Eqs. (36) and (37). $R_x(t)$ and $R_y(t)$ are the x- and y-component forces, respectively, exerted by the point constraint on the elastica

during vibration. $\delta(\cdot)$ is the dimensionless Dirac delta function. For an elastica element not involving the point constraint, the delta functions in Eqs. (36) and (37) are neglected.

We denote the static solutions of Eqs. (33)–(38) as $x_e(s)$, $y_e(s)$, $\theta_e(s)$, $M_e(s)$, $F_{xe}(s)$, and $F_{ye}(s)$. These static solutions have been obtained in Sec. 3. In the case when contact occurs, the relations between F_{xe}, F_{ye} and F_A, Q_A are

$$F_{xe}(s) = -F_A + R_{xe}H(s-l_1) \tag{39}$$

$$F_{ye}(s) = Q_A + R_{ye}H(s-l_1) \tag{40}$$

where H is the Heaviside step function. It is noted that in Eq. (39), F_A is an external pushing force, which is conventionally denoted as positive in buckling analysis. On the other hand, F_{xe} is an internal force, which follows the usual sign convention similar to the stress tensor notation, as shown in Fig. 3. During vibration, the function $F_x(s,t)$ may be regarded as the superposition of $F_{xe}(s)$ and a small perturbation, expressed mathematically as

$$F_x(s,t) = F_{xe}(s) + [R_{xe}(H(s-l_1-\eta_1) - H(s-l_1))] + [F_{xd}(s-\eta_1) + R_{xd}H(s-l_1-\eta_1)]\sin\,\omega t \tag{41}$$

where ω is a natural frequency of the constrained elastica. A variable with subscript "d" represents a small perturbation of its static counterpart with subscript "e." The first bracket on the right hand side of Eq. (41) represents the shift of the contact point from $s=l_1$ to $s=l_1+\eta_1$. After using Eq. (39), Eq. (41) can be rewritten as

$$F_x(s,t) = F_{xe}(s-\eta_1) + [F_{xd}(s-\eta_1) + R_{xd}H(s-l_1-\eta_1)]\sin\,\omega t \tag{42}$$

After defining a new variable ε as

$$\varepsilon = s - \eta_1 \tag{43}$$

Equation (42) can be rewritten as

$$\hat{F}_x(\varepsilon,t) = F_{xe}(\varepsilon) + [F_{xd}(\varepsilon) + R_{xd}H(\varepsilon-l_1)]\sin\,\omega t \tag{44}$$

where $\hat{F}_x(\varepsilon,t) = F_x(\varepsilon+\eta_1,t)$. Apparently, $\hat{F}_x$ and F_x are two different functions. It is noted that $F_{xe}(\varepsilon)$ is the static solution as obtained from the previous static analysis, except that the independent variable s (as appeared in Eq. (39)) is replaced by ε. Similarly, the other perturbed functions may be written as

$$\hat{F}_y(\varepsilon,t) = F_{ye}(\varepsilon) + [F_{yd}(\varepsilon) + R_{yd}H(\varepsilon-l_1)]\sin\,\omega t \tag{45}$$

$$\hat{x}(\varepsilon,t) = x_e(\varepsilon) + x_d(\varepsilon)\sin\,\omega t \tag{46}$$

$$\hat{y}(\varepsilon,t) = y_e(\varepsilon) + y_d(\varepsilon)\sin\,\omega t \tag{47}$$

$$\hat{\theta}(\varepsilon,t) = \theta_e(\varepsilon) + \theta_d(\varepsilon)\sin\,\omega t \tag{48}$$

$$\hat{M}(\varepsilon,t) = M_e(\varepsilon) + M_d(\varepsilon)\sin\,\omega t \tag{49}$$

ε defined in Eq. (43) may be called the Eulerian coordinate of a point on the elastica. $\varepsilon=l_1$ represents the point of the elastica passing through the point constraint at any instance during vibration. It can be a different material point at a different instant. The physical meaning of $\varepsilon=l_1$ is like fixing a control window at the point constraint. Therefore, we call this type of description an Eulerian one.

By noting that $\partial\varepsilon/\partial s=1$, the Lagrangian version of the governing equations (Eqs. (33)–(38)) can now be transformed into the Eulerian version as

$$\frac{\partial\hat{x}(\varepsilon,t)}{\partial\varepsilon} = \cos\,\hat{\theta}(\varepsilon,t) \tag{50}$$

$$\frac{\partial\hat{y}(\varepsilon,t)}{\partial\varepsilon} = \sin\,\hat{\theta}(\varepsilon,t) \tag{51}$$

$$\frac{\partial\hat{M}(\varepsilon,t)}{\partial\varepsilon} = \hat{F}_x(\varepsilon,t)\sin\,\hat{\theta}(\varepsilon,t) - \hat{F}_y(\varepsilon,t)\cos\,\hat{\theta}(\varepsilon,t) \tag{52}$$

$$\frac{\partial\hat{F}_x(\varepsilon,t)}{\partial\varepsilon} - R_x(t)\,\delta(\varepsilon-l_1) = \frac{1}{4\pi^2}\frac{\partial^2\hat{x}(\varepsilon,t)}{\partial t^2} \tag{53}$$

$$\frac{\partial\hat{F}_y(\varepsilon,t)}{\partial\varepsilon} - R_y(t)\,\delta(\varepsilon-l_1) = \frac{1}{4\pi^2}\frac{\partial^2\hat{y}(\varepsilon,t)}{\partial t^2} \tag{54}$$

$$\frac{\partial\hat{\theta}(\varepsilon,t)}{\partial\varepsilon} = 4\pi^2\hat{M}(\varepsilon,t) \tag{55}$$

By substituting Eqs. (44)–(49), together with the relations

$$R_x(t) = R_{xe} + R_{xd}\sin\,\omega t \tag{56}$$

$$R_y(t) = R_{ye} + R_{yd}\sin\,\omega t \tag{57}$$

$$\eta_1(t) = \eta_{1d}\sin\,\omega t \tag{58}$$

into Eqs. (50)–(55) and ignoring the higher-order terms, we arrive at the following linear equations for the six functions $x_d(\varepsilon)$, $y_d(\varepsilon)$, $\theta_d(\varepsilon)$, $M_d(\varepsilon)$, $F_{xd}(\varepsilon)$, and $F_{yd}(\varepsilon)$:

$$\frac{dx_d(\varepsilon)}{d\varepsilon} = -\theta_d(\varepsilon)\sin\,\theta_e(\varepsilon) \tag{59}$$

$$\frac{dy_d(\varepsilon)}{d\varepsilon} = \theta_d(\varepsilon)\cos\,\theta_e(\varepsilon) \tag{60}$$

$$\frac{d\theta_d(\varepsilon)}{d\varepsilon} = 4\pi^2 M_d(\varepsilon) \tag{61}$$

$$\frac{dM_d(\varepsilon)}{d\varepsilon} = [F_{xe}(\varepsilon)\theta_d(\varepsilon) - F_{yd}(\varepsilon) - R_{yd}H(\varepsilon-l_1)]\cos\,\theta_e(\varepsilon) + [F_{ye}(\varepsilon)\theta_d(\varepsilon) + F_{xd}(\varepsilon) + R_{xd}H(\varepsilon-l_1)]\sin\,\theta_e(\varepsilon) \tag{62}$$

$$\frac{dF_{xd}(\varepsilon)}{d\varepsilon} = -\frac{1}{4\pi^2}\omega^2[x_d(\varepsilon) - \cos\,\theta_e(\varepsilon)\,\eta_{1d}] \tag{63}$$

$$\frac{dF_{yd}(\varepsilon)}{d\varepsilon} = -\frac{1}{4\pi^2}\omega^2[y_d(\varepsilon) - \sin\,\theta_e(\varepsilon)\,\eta_{1d}] \tag{64}$$

4.2 Boundary Conditions. The exact boundary conditions at fixed end B are

$$x(s,t)\big|_{s=l} = \hat{x}(\varepsilon,t)\big|_{\varepsilon=l-\eta_1} = 1 \tag{65}$$

$$y(s,t)\big|_{s=l} = \hat{y}(\varepsilon,t)\big|_{\varepsilon=l-\eta_1} = 0 \tag{66}$$

$$\theta(s,t)\big|_{s=l} = \hat{\theta}(\varepsilon,t)\big|_{\varepsilon=l-\eta_1} = 0 \tag{67}$$

These boundary conditions can be linearized as follows. Take Eq. (65) as an example. By using Eq. (46), we can rewrite Eq. (65) into

$$x_e(\varepsilon)\big|_{\varepsilon=l-\eta_1} + x_d(\varepsilon)\big|_{\varepsilon=l-\eta_1}\sin\,\omega t = 1 \tag{68}$$

Both $x_e(\varepsilon)\big|_{\varepsilon=l-\eta_1}$ and $x_d(\varepsilon)\big|_{\varepsilon=l-\eta_1}$ in Eq. (68) can be expanded as a Taylor series with respect to $\varepsilon=l$. After ignoring the higher-order terms, Eq. (68) can be linearized to

$$x_d(\varepsilon)\big|_{\varepsilon=l} = \eta_{1d} \tag{69}$$

Similarly, the boundary conditions (66) and (67) can be linearized to

$$y_d(\varepsilon)\big|_{\varepsilon=l} = 0 \tag{70}$$

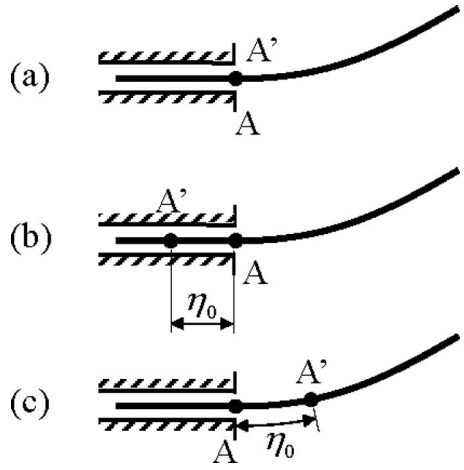

Fig. 4 The boundary conditions at the opening A of the feeding channel. (*a*) In equilibrium position, the material point *A′* coincides with point A. When the elastica vibrates, the material point *A′* (*b*) retreats in and (*c*) protrudes out of the channel.

$$\theta_d(\varepsilon)|_{\varepsilon=l} = 4\pi^2 M_e(\varepsilon)|_{\varepsilon=l}\eta_{1d} \tag{71}$$

The boundary condition on the left end A is more complicated. We denote the material point on the strip right at the opening A of the channel as point A' when the elastica is in equilibrium, as shown in Fig. 4(*a*). Since the strip is under a constant pushing force at the left end, A' will retreat into and protrude out of the channel when the elastica vibrates, as shown in Figs. 4(*b*) and 4(*c*). We denote this small length of movement as

$$\eta_0(t) = \eta_{0d}\sin\omega t \tag{72}$$

The condition of zero slope at opening A requires that

$$\theta(s,t)|_{s=\eta_0} = \hat{\theta}(\varepsilon,t)|_{\varepsilon=\eta_0-\eta_1} = 0 \tag{73}$$

Following the similar linearization procedure as that in point B, we can linearize the boundary condition (73) to the form

$$\theta_d(\varepsilon)|_{\varepsilon=0} = -4\pi^2 M_e(\varepsilon)|_{\varepsilon=0}(\eta_{0d} - \eta_{1d}) \tag{74}$$

Similarly, we can derive

$$x_d(\varepsilon)|_{\varepsilon=0} = -(\eta_{0d} - \eta_{1d}) \tag{75}$$

$$y_d(\varepsilon)|_{\varepsilon=0} = 0 \tag{76}$$

$$F_{xd}(\varepsilon)|_{\varepsilon=0} = 0 \tag{77}$$

Finally, Eqs. (74) and (75) may be combined as

$$\theta_d(\varepsilon)|_{\varepsilon=0} = 4\pi^2 M_e(\varepsilon)|_{\varepsilon=0}x_d(\varepsilon)|_{\varepsilon=0} \tag{78}$$

The three equations (Eqs. (76)–(78)) are the linearized boundary conditions in point A.

4.3 Constraint Equations. When contact occurs, we require that the elastica always passes through the point constraint. Mathematically, this condition can be written as

$$x(s,t)|_{s=l_1+\eta_1} = \hat{x}(\varepsilon,t)|_{\varepsilon=l_1} = 0.5 \tag{79}$$

$$y(s,t)|_{s=l_1+\eta_1} = \hat{y}(\varepsilon,t)|_{\varepsilon=l_1} = h \tag{80}$$

After using Eqs. (46) and (47), Eqs. (79) and (80) can be rewritten as

$$x_d(\varepsilon)|_{\varepsilon=l_1} = 0 \tag{81}$$

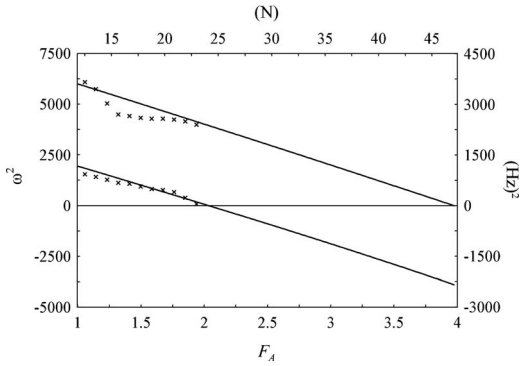

Fig. 5 ω^2 of the first two modes as functions of the end force F_A for deformation (2). The cross marks × represent the experimental measurements.

$$y_d(\varepsilon)|_{\varepsilon=l_1} = 0 \tag{82}$$

We also require that the dynamic reactive force must be always normal to the elastica at the point constraint, or mathematically,

$$R_x\cos\hat{\theta}(\varepsilon,t) + R_y\sin\hat{\theta}(\varepsilon,t) = 0 \quad \text{at} \quad \varepsilon = l_1 \tag{83}$$

After using Eqs. (48), (56), and (57) and neglecting higher-order terms, Eq. (83) can be linearized to

$$[R_{ye}\theta_d(\varepsilon) + R_{xd}]\cos\theta_e(\varepsilon) + [-R_{xe}\theta_d(\varepsilon) + R_{yd}]\sin\theta_e(\varepsilon) = 0 \quad \text{at} \quad \varepsilon = l_1 \tag{84}$$

Equations (81), (82), and (84) are the three constraint equations.

4.4 Solution Method. In summary, the six linearized differential equations (Eqs. (59)–(64)), six boundary conditions (Eqs. (69)–(71) and (76)–(78)), and three constraint equations (Eqs. (81), (82), and (84)) admit nontrivial solutions only when ω is equal to an eigenvalue of the system of equations. The unknowns found are the six functions $x_d(\varepsilon)$, $y_d(\varepsilon)$, $\theta_d(\varepsilon)$, $M_d(\varepsilon)$, $F_{xd}(\varepsilon)$, $F_{yd}(\varepsilon)$, the amplitude of sliding at the point constraint η_{1d}, and the two dynamic constraint reactions R_{xd} and R_{yd}. It is noted that ω in Eqs. (63) and (64) only appears in the form of ω^2. Therefore, if the characteristic value ω^2 is positive, the corresponding mode is stable with natural frequency ω. On the other hand, the equilibrium configuration is unstable if ω^2 is negative.

A shooting method is used to solve for the characteristic value ω^2. We first set $M_d(\varepsilon)|_{\varepsilon=0}=1$. After guessing six variables $x_d(\varepsilon)|_{\varepsilon=0}$, $F_{yd}(\varepsilon)|_{\varepsilon=0}$, R_{xd}, R_{yd}, η_{1d}, and ω^2, we can integrate the homogeneous Eqs. (59)–(64) like an initial value problem all the way from $\varepsilon=0$ to $\varepsilon=l$. The three boundary conditions (Eq. (69)–(71)) at $\varepsilon=l$ and the three constraint equations (Eqs. (81), (82), and (84)) at $\varepsilon=l_1$ are used to check the accuracy of the guesses. If the guesses are not satisfactory, a new set of guesses is adopted. A Newton–Raphson's method is employed to improve the iteration speed. The stability of the deformations in Fig. 2 is determined in this manner.

Figure 5 shows ω^2 of the first two modes as functions of the end force F_A for deformation (2). The ω^2 of the first mode becomes negative when F_A reaches 2.03268 at which the symmetry-breaking bifurcation occurs. It is noted that the ω^2 of the second mode becomes negative when F_A reaches 3.97314. This happens to be the point in which deformation (3) begins to appear.

The first two mode shapes when $F_A=1.5$ are depicted in Fig. 6. The solid and dashed curves represent the static and the vibrating mode shapes of the constrained elastica. The first mode (a) is asymmetric and the second mode (b) is symmetric. To examine whether sliding at the contact point occurs we examine the values of η_{0d} and η_{1d} of each mode. For the asymmetric mode we found that the ratio η_{0d}/η_{1d} is approximately 1:400. This means that

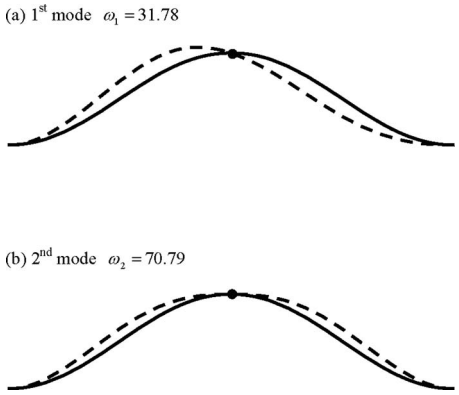

Fig. 6 The first two mode shapes of the constrained elastica when $F_A = 1.5$

during vibration the protruding and retreating of the elastica at the channel opening A is negligible compared with the sliding at the contact point. In other words, the elastica length within the domain of interest is almost constant during vibration. This can also be observed from Fig. 6(*a*). For the symmetric mode, we found that the ratio η_{0d}/η_{1d} is approximately 2:1. Therefore, sliding at the contact point still occurs. From Fig. 6(*b*) we can observe that the lengths of the elastica on both sides of the point constraint increase (or decrease during the other half of the vibration period) the same amount. Since the elastica is inextensible, the protruding η_{0d} at the channel opening has to be twice the amount of the sliding η_{1d} at the contact point. A vibration analysis of a constrained structure will cause an erroneous result if sliding at the constraint is neglected.

It is noted that the geometric conditions (81) and (82) at the point constraint are exact. Therefore, the vibrating elastica always passes through the point constraint no matter how large the vibration amplitude is. On the other hand, the boundary conditions in points A and B used in the calculation have been linearized from the exact boundary conditions. Therefore, the mode shapes do not necessarily satisfy the exact boundary conditions in points A and B. This may become obvious when the amplitude of vibration is increased dramatically.

5 Experimental Observations

In order to examine the above theoretical predictions, we designed an experimental apparatus, whose top-view is shown in Fig. 7. The elastica is made of stainless steel (AISI type 420) with Young's modulus 200 GPa and mass density 7800 kg/m^3. The cross section of the elastica is 60×0.3 mm^2. The right end of the strip is fully clamped in an aluminum block, which corresponds to point B in Fig. 1. To simulate the partial clamp on the left end of the domain of interest, we install two pairs of rollers in another aluminum block. This design ensures that the strip in the partial clamp remains straight before it is fed through point A. The rollers are to minimize the friction between the strip and the feeding channel. The distance between point A (at the center position of the pair of rollers closer to the point constraint) and point B is 30 cm. The left end of the strip is fully clamped in a slider, which is

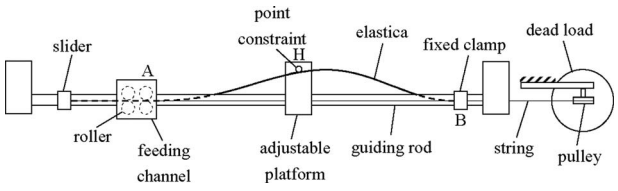

Fig. 7 Top view of the experimental apparatus

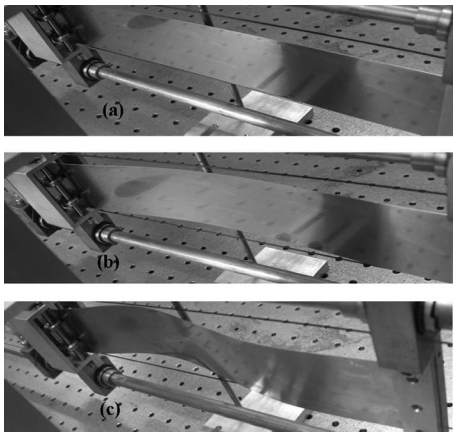

Fig. 8 Photographs of (*a*) straight configuration before Euler buckling, (*b*) deformation (2), and (*c*) deformation (4)

allowed to slide along a set of guiding rods. Two strings are attached to this slider, one on the top and the other on the bottom. The strings pass through two pulleys with the other end attached to a hanging bucket weighing 100 g. Steel screws, each weighs 106.6 g, are added to the bucket to simulate the pushing force on the left end of the strip. As a result, this is a load-control experiment instead of a displacement-control procedure as in Ref. [9]. The point constraint is made of a steel rod of circular cross section with 5 mm of diameter. One end of the steel rod is screwed onto an aluminum platform whose position can be easily adjusted.

The measured relations between F_A and Δl are plotted with cross marks $\times$ in Fig. 2. For convenient reference, we add the physical parameters with units of F_A and Δl on the right and top sides of the diagram. At the last point before a jump occurs, the cross mark is circled. As expected, the theoretical sharp turn at the buckling point $F_A = 1$ is replaced by a smooth curve due to geometrical imperfection of the strip. In the experiment, the first jump occurs at $F_A = 0.878$. The discrepancy between theory and experiment is 12.2%. In reading this experimental data, we have to take into account the fact that the increment of F_A in the experiment is 0.088. Therefore, if we take the point after the jump occurs as the snapping load, instead of the circled one as described above, the discrepancy will become as small as 3.6%.

After the first jump, the strip is in contact with the point constraint. The length increment Δl at this point is measured as 0.00233, compared with the theoretical prediction 0.0022188. As the force F_A continues to increase, the load-deflection relation follows a smooth curve instead of a sharp turn at the symmetry-breaking bifurcation point as predicted by theory. Gradually the elastica evolves to deformation (4a) until the second jump occurs at $(F_A, \Delta l) = (1.673, 0.00343)$, which is also circled in Fig. 2. This represents a 17.8% discrepancy in snapping force compared with the theoretical prediction $F_A = 2.03554$. After the second jump, the clamping slider at the left end of the strip will hit the left side of the aluminum block containing the two pairs of rollers. The longest strip we have at hand in the experiment is 1 m long. In other words, the longest dimensionless length increment Δl we can handle in the experiment is 2.33. This prevents us from demonstrating the self-contact configuration as mentioned in Sec. 3.5. In Fig. 8 we show photographs of a series of different deformations we have observed in the experiment. Figure 8(*a*) shows the straight configuration before the Euler buckling occurs. Figures 8(*b*) and 8(*c*) show the symmetric deformation (2) and the asymmetric deformation (4a), respectively.

Although the agreement between the experiment and the theory is not as good as we desire, it is safe to say that the experimental load-deflection curve follows the theoretical one qualitatively. The discrepancy is believed to be due to the geometrical imperfection

of the experimental set-up and friction at the point constraint and the feeding channel. These inevitable imperfections in reality spoil the assumption of perfect geometry and frictionless condition adopted in the theory.

The natural frequencies of the constrained elastica can be measured using a photonic sensor (MTI-2000). The noncontact photonic probe shines a beam of light perpendicularly onto the surface of the strip at somewhere near the middle point. The strip is hit by a small object simulating an impact. From the power spectrum of the response, which was collected and calculated with a spectrum analyzer, we can identify some of the lowest natural frequencies. The cross marks in Fig. 5 represent the square of the first two measured natural frequencies of deformation (2). It is noted that the measured fundamental frequency agrees very well with the theoretical prediction before the symmetry-breaking bifurcation occurs. This agreement enhances our confidence in the validity of the vibration and stability theories presented in Sec. 4.

6 Conclusions

This paper studies the deformation and stability of an elastica constrained by a point in the middle with clearance. One end of the elastica is fully clamped while the other end is allowed to slide without friction and clearance inside a rigid channel. The point constraint is slightly above the base line of the clamps. The elastica is compressed by a longitudinal force causing it to buckle in the domain of interest between the full clamp and the opening of the feeding channel. Emphasis is placed on the interaction of the loaded elastica and the point constraint. The theoretical predictions are examined by a load-control experiment. Some of the conclusions can be summarized as follows.

(1) The elastic strip buckles when the pushing force reaches the conventional buckling load. At this buckling load, a subcritical bifurcation occurs with the nontrivial equilibrium path falling as the pushing force increases. It is noted that this type of subcritical bifurcation is due to the variable-length feature of the elastica as studied in this paper. A similar phenomenon was reported in other studies on variable-length elastica [10,11]. A column with fixed length, on the other hand, will buckle via a supercritical bifurcation with the nontrivial equilibrium path rising as the load increases. There will be no jump in the fixed length problem.
(2) After the subcritical bifurcation, the elastica jumps to a symmetric configuration in contact with the point constraint. As the pushing force increases further, a symmetry-breaking bifurcation occurs and the elastica evolves to one of a pair of asymmetric deformations. As the pushing force continues to increase, the asymmetric deformation experiences a second jump to a self-contact configuration.
(3) In order to take into account the sliding between the elastica and the point constraint during vibration, a vibration analysis based on an Eulerian description is adopted. After transforming the governing equations and the boundary conditions from the Lagrangian description to the Eulerian one, the natural frequencies of the constrained elastica can be calculated and the stability can be determined.
(4) The experiment confirms the two jumps and the symmetry-breaking bifurcation predicted theoretically. The experimental load-deflection curve follows the theoretical one qualitatively. However, the agreement is not as good as we desire. The discrepancy between the experimental and theoretical load-deflection curves is believed to be due to the geometrical imperfection of the experimental set-up and the frictions at the point constraint and the feeding channel.

References

[1] Love, A. E., 1944, *A Treatise on the Mathematical Theory of Elasticity*, Dover, New York.
[2] Domokos, G., Holmes, P., and Royce, B., 1997, "Constrained Euler Buckling," J. Nonlinear Sci., **7**, pp. 281–314.
[3] Holmes, P., Domokos, G., Schmitt, J., and Szeberenyi, I., 1999, "Constrained Euler Buckling: An Interplay of Computation and Analysis," Comput. Methods Appl. Mech. Eng., **170**, pp. 175–207.
[4] Plaut, R. H., Taylor, R. P., and Dillard, D. A., 2004, "Postbuckling and Vibration of a Flexible Strip Clamped at Its Ends to a Hinged Substrate," Int. J. Solids Struct., **41**, pp. 859–870.
[5] Chai, H., 2002, "On the Post-Buckling Behavior of Bilaterally Constrained Plates," Int. J. Solids Struct., **39**, pp. 2911–2926.
[6] Chai, H., 2006, "On the Crush Worthiness of a Laterally Confined Bar Under Axial Compression," ASME J. Appl. Mech., **73**, pp. 834–841.
[7] Roman, B., and Pocheau, A., 2002, "Postbuckling of Bilaterally Constrained Rectangular Thin Plates," J. Mech. Phys. Solids, **50**, pp. 2379–2401.
[8] Chen, J.-S., and Li, C.-W., 2007, "Planar Elastica Inside a Curved Tube With Clearance," Int. J. Solids Struct., **44**, pp. 6173–6186.
[9] Lu, Z.-H., and Chen, J.-S., 2008, "Deformations of a Clamped-Clamped Elastica Inside a Circular Channel With Clearance," Int. J. Solids Struct., **45**, pp. 2470–2492.
[10] Wang, C. M., Lam, K. Y., and He, X. Q., 1998, "Instability of Variable-Arc-Length Elastica Under Follower Force," Mech. Res. Commun., **25**, pp. 189–194.
[11] Chucheepsakul, S., and Monprapussorn, T., 2000, "Divergence Instability of Variable-Arc-Length Elastica Pipes Transporting Fluid," J. Fluids Struct., **14**, pp. 895–916.
[12] Hartono, W., 2000, "Behavior of Variable Length Elastica With Frictional Support Under Follower Force," Mech. Res. Commun., **27**, pp. 653–658.
[13] Pulngern, T., Chucheepsakul, S., and Halling, M. W., 2005, "Analytical and Experimental Studies on the Large Amplitude Vibrations of Variable-Arc-Length Beams," J. Vib. Control, **11**, pp. 923–947.
[14] Burgess, I. W., 1971, "On the Equilibrium and Stability of Discrete One-Way Structural Systems," Int. J. Solids Struct., **7**, pp. 667–683.
[15] Godoy, L. A., and Mirasso, A. E., 2003, "On the Elastic Stability of Static Non-Holonomic Systems," Int. J. Solids Struct., **40**, pp. 3439–3462.